Electronic Supplementary Material (ESI) for Nanoscale.

Supporting Information

Ternary dendritic nanowires as highly active and stable multifunctional electrocatalysts

Yoojin Yang, Haneul Jin, Ho Young Kim, Jisun Yoon, Jongsik Park, Hionsuck Baik,* Sang Hoon Joo,* and Kwangyeol Lee*

Experimental Section

Reagents. $Pt(acac)_2$ (97%), $Ni(acac)_2$ (95%), $Mo(CO)_6$ (≥99.9% trace metals basis), and oleylamine (≥98%) were purchased from Sigma-Aldrich. All reagents were used as received without further purification.

Preparation of barbed wire-like, dendritic Mo-doped PtNi nanostructure (Mo-PtNi DNW).

A slurry of platinum(II) acetylacetonate ($Pt(acac)_2$, 0.05 mmol, Sigma-Aldrich, 97%), nickel(II) acetylacetonate ($Ni(acac)_2$, 0.05 mmol, Sigma-Aldrich, 95%), and molybdenum hexacarbonyl ($Mo(CO)_6$, 0.005 mmol, Sigma-Aldrich, ≥99.9% trace metals basis) in oleylamine (6 mmol, OAm, Sigma-Aldrich, ≥98%) was prepared in a 100 mL Schlenk tube with magnetic stirring. After being placed under vacuum 5 min, the solution was charged with 1 atm Ar gas, followed by an aging step at 80 ºC for 5 h, which forms Pt nanowires. After the aging step, the reaction mixture was rapidly heated up to 180 ^oC at a heating rate of 11.5 $^oC\ min^{-1}$ and was kept at that temperature for 1 h. The reaction mixture was cooled down to room temperature and washed several times with toluene and methanol to form precipitates that were collected by centrifugal separation.

Preparation of Barbed wire-like, dendritic Mo-doped Pt nanostructure (Mo-Pt DNW).

The same synthetic process as above was used without nickel(II) acetylacetonate ($Ni(acac)_2$) in the reaction mixture.

Preparation of Mo-PtNi DNW and Mo-Pt DNW on carbon

For the electrocatalytic measurement, carbon black (Vulcan XC-72R) powder and as-prepared nanoparticles were put into a 70 mL vial with 10 mL of toluene and a 50 mL conical tube with 5 mL of toluene, respectively, and sonicated for 10 minutes. After 10 minutes, the slurry of nanoparticles was poured into the 70 mL vial containing carbon black, and the combined slurry was sonicated for additional 3 minutes. The resultant slurry was transferred to a 50 mL conical tube, and 20 mL of acetone was added for washing. The nanoparticles loaded on carbon black were separated by centrifugation and then dried in an oven for 24 hours.

Material chracterization

TEM and HRTEM studies were carried out in a Tecnai G2 F30ST microscope and Tecnai G2 20 S-twin microscope. Aberration-corrected imaging and high spatial resolution EDS were performed at FEI Nanoport in Eindhoven using a Titan Probe Cs TEM 300kV with Chemi-STEM technology. EDS elemental mapping data were collected using a higher efficiency detection system (Super-X detector with XFEG); it integrates 4 FEI-designed Silicon Drift Detectors (SDDs) very close to the sample area. Compared to conventional EDX detector with Schottky FEG systems, ChemiSTEM produces up to 5 times the X-ray generation with the X-FEG, and up to 10 times the X-ray collection with the Super-X detector. X-ray diffraction (XRD) patterns were collected with a Rigaku Ultima III diffractometer system using a graphite-monochromatized Cu-Kα radiation at 40 kV and 30 mA. Metal contents were determined by inductively coupled plasma-optical emission spectrometry (ICP-OES).

Electrochemical chracterization.

Rotating disk electrode (RDE, ALS) half-cell tests were conducted using an IviumStat electrochemical analyzer. All the measurements were carried out at room temperature using a three-compartment electrochemical cell. The working electrode was prepared by deposition of ethanol-based catalyst dispersion onto the glassy carbon electrode of the RDE. The catalyst dispersion was prepared by ultrasonication-assisted mixing of the catalyst, deionized water, 5 wt% Nafion and ethanol for at least 30 min in an ice bath. The deposited catalysts dispersion was dried at 70 °C for 2 min. All potentials are relative to RHE, with a graphite rod used as a counter electrode. Prior to electrochemical measurements, 50 potential cycles from 0.05 to 1.2 V at a scan rate of 500 mV s^{-1} were conducted in a N_2-saturated 0.1 M $HClO_4$ solution for electrochemical cleaning. The cyclic voltammograms were obtained under the same conditions as above, except that the scan rate was changed to 50 mV s^{-1} for 3 cycles. The electrochemically active surface area (ECSA) was estimated by carbon monoxide (CO) stripping method (CO_{ad}). The CO stripping measurements were performed by purging CO through the electrolyte while holding the potential at 0.05 V. N_2 was then purged to remove CO from the electrolyte and the CV was collected at a sweep rate of 50 mV s^{-1}.

The evaluation for the methanol oxidation reaction (MOR) were obtained with potential cycling from 0.05 to 1.2 V at a scan rate of 50 mV s^{-1} were conducted in a N_2-saturated 0.1 M $HClO_4$ + 1 M CH_3OH solution, using cyclic voltammetry (CV). Accelerated degradation tests (ADTs) were conducted in N_2-saturated 0.1 M $HClO_4$ + 1 M CH_3OH solution with chronoamperometry, at a potential of 0.9 V vs RHE. Additionally, ADTs were conducted in N_2-saturated 0.1 M $HClO_4$ + 1 M CH_3OH solution in a potential range from 0.05 to 1.2 V vs RHE at a scan rate of 50 mV s^{-1} for 500 cycles. After the cycling, the MOR activity was measured in fresh electrolyte. The MOR curves before and after potential cycling were obtained under the same conditions as the ones used for the above MOR measurement.

Linear sweep voltammetry (LSV) curves for the oxygen reduction reaction (ORR) were obtained using a potential sweep from –0.01 to 1.1 V in an O_2-saturated 0.1 M $HClO_4$ solution with O_2 purging at a rotation speed of 1600 rpm and a scan rate of 20 mV s^{-1}. Currents were collected after iR-drop correction. ADTs were conducted in N_2-saturated 0.1 M $HClO_4$ solution in a potential range from 0.6 to 1.0 V vs RHE at a scan rate of 50 mV s^{-1} for 10,000 cycles. After the cycling, the ORR activity was measured in fresh electrolyte. The ORR polarization curves before and after potential cycling were obtained under the same conditions as the ones used for the above ORR measurement.

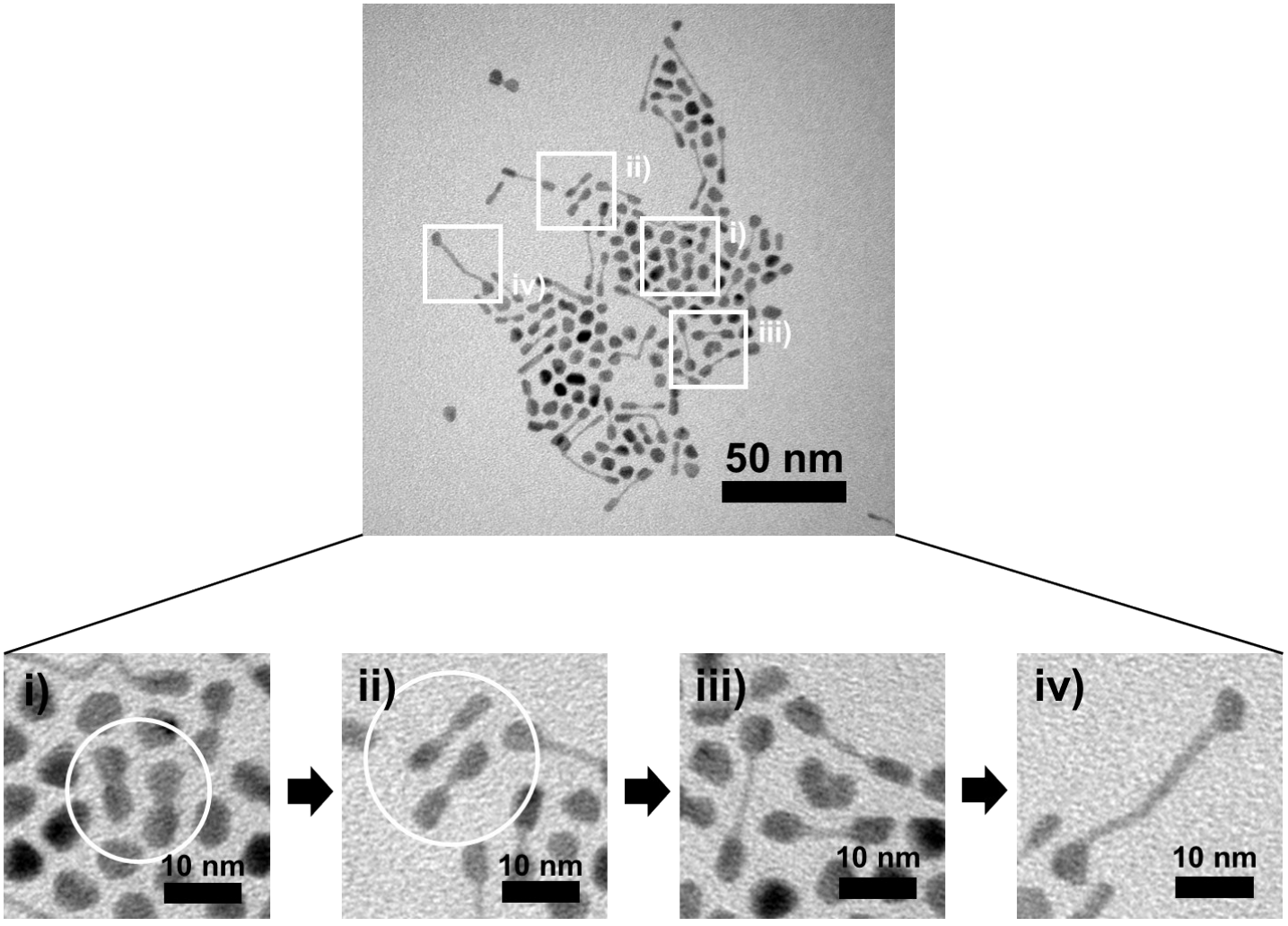

Fig. S1. TEM images of early stage intermediates of the aging step, demonstrating the growth mechanism of Pt nanowire with two Pt heads. The images in (i)-(iv) are found at the same reaction time, but are organized in the order of increasing nanowire lengths.

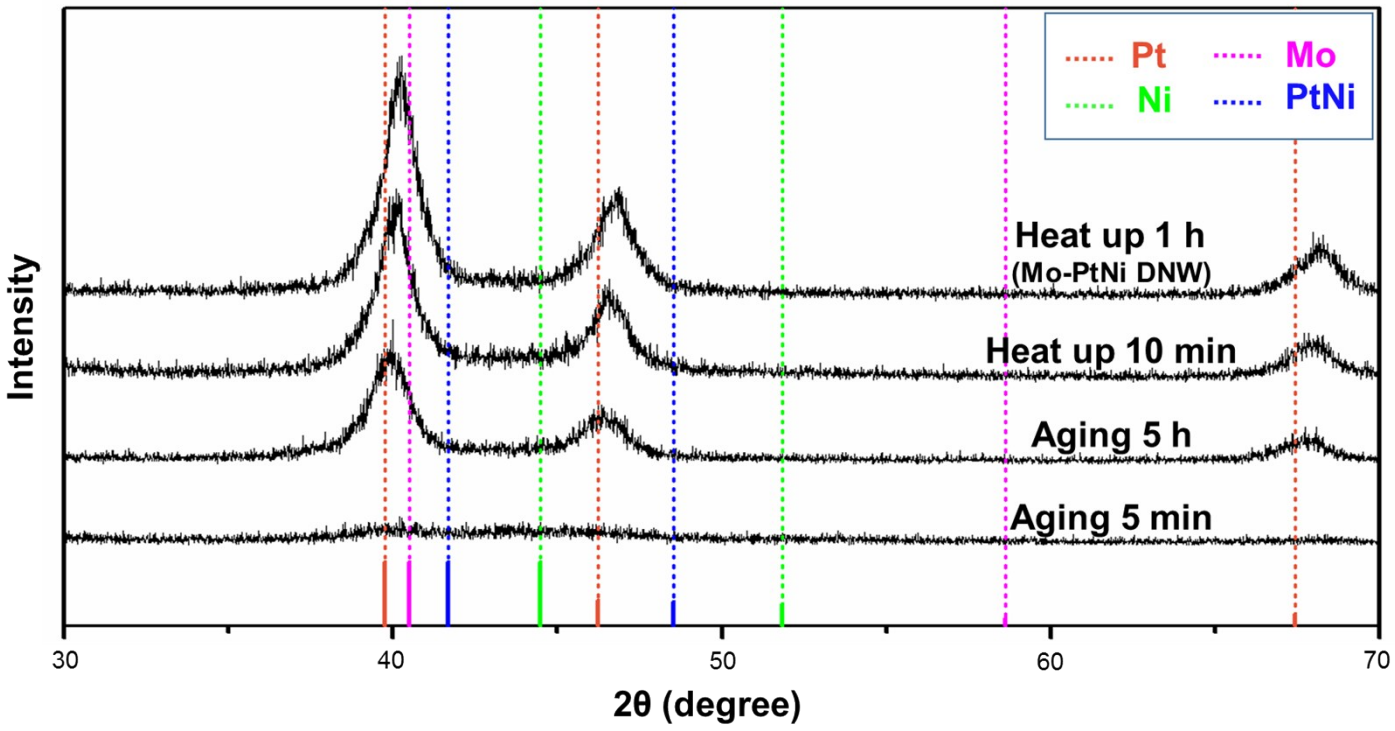

Fig. S2. Powder X-ray diffraction patterns (PXRD) of reaction intermediates at 5 min aging at 80 °C, 5 h aging at 80 °C, 10 min after heating at 180 °C, and 1 h after heating at 180 °C. (Pt (JCPDS no.01-071-3756), Ni (JCPDS no.01-071-3740), PtNi (JCPDS no.01-072-2525), Mo (JCPDS no.01-089-5156))

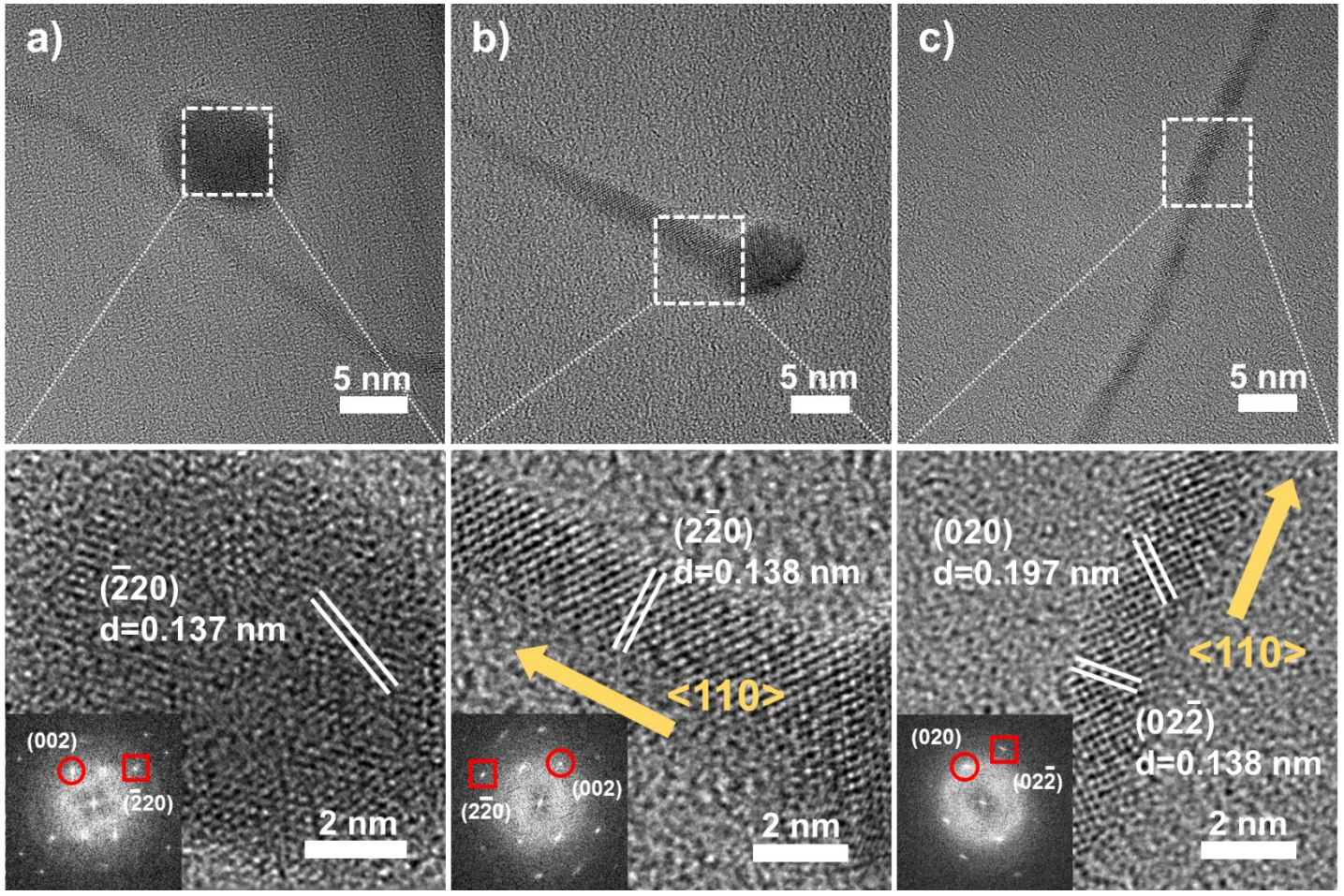

Fig. S3. HRTEM images of intermediate nanoparticles at the early stage of aging at 80 °C; a) an un-halved nanoparticle, b) head part of a nanowire, c) stem part of a nanowire, accompanied by their corresponding FFT patterns. Both d-spacing values and elemental mapping (in Figure S4) indicate the intermediates are mostly composed of Pt. The growth direction of wire is <110>.

	Pt (at. %)	Ni (at. %)
Aging 5 min	99.97	0.03
Aging 5 h	99.02	0.98
Heat up 10 min	88.27	11.73
Heat up 1h (Mo-PtNi DNW)	62.13	37.87

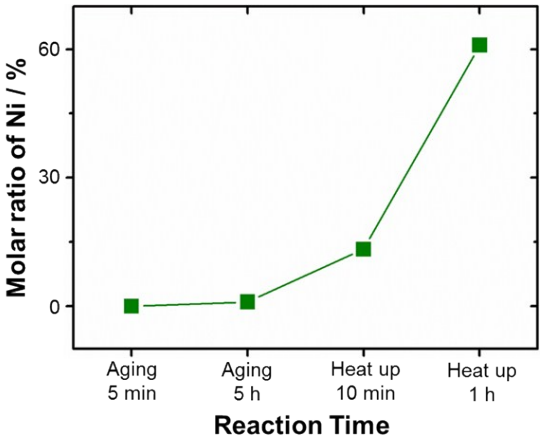

Fig. S4. Energy-dispersive X-ray spectroscopy (EDS) analysis of intermediates at 5 min aging at 80 °C, 5 h aging at 80 °C, 10 min after heating at 180 °C, and 1 h after heating at 180 °C.

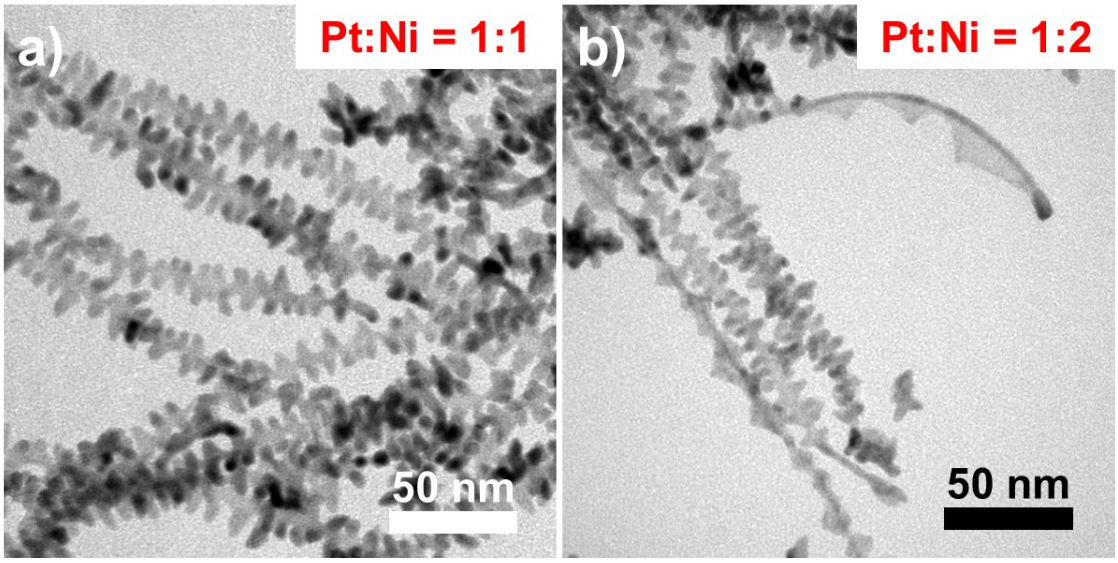

Fig. S5. Barbed-like wire structure obtained by varying the amount of $Ni(acac)_2$; a) 0.05 mmol and b) 0.1 mmol.

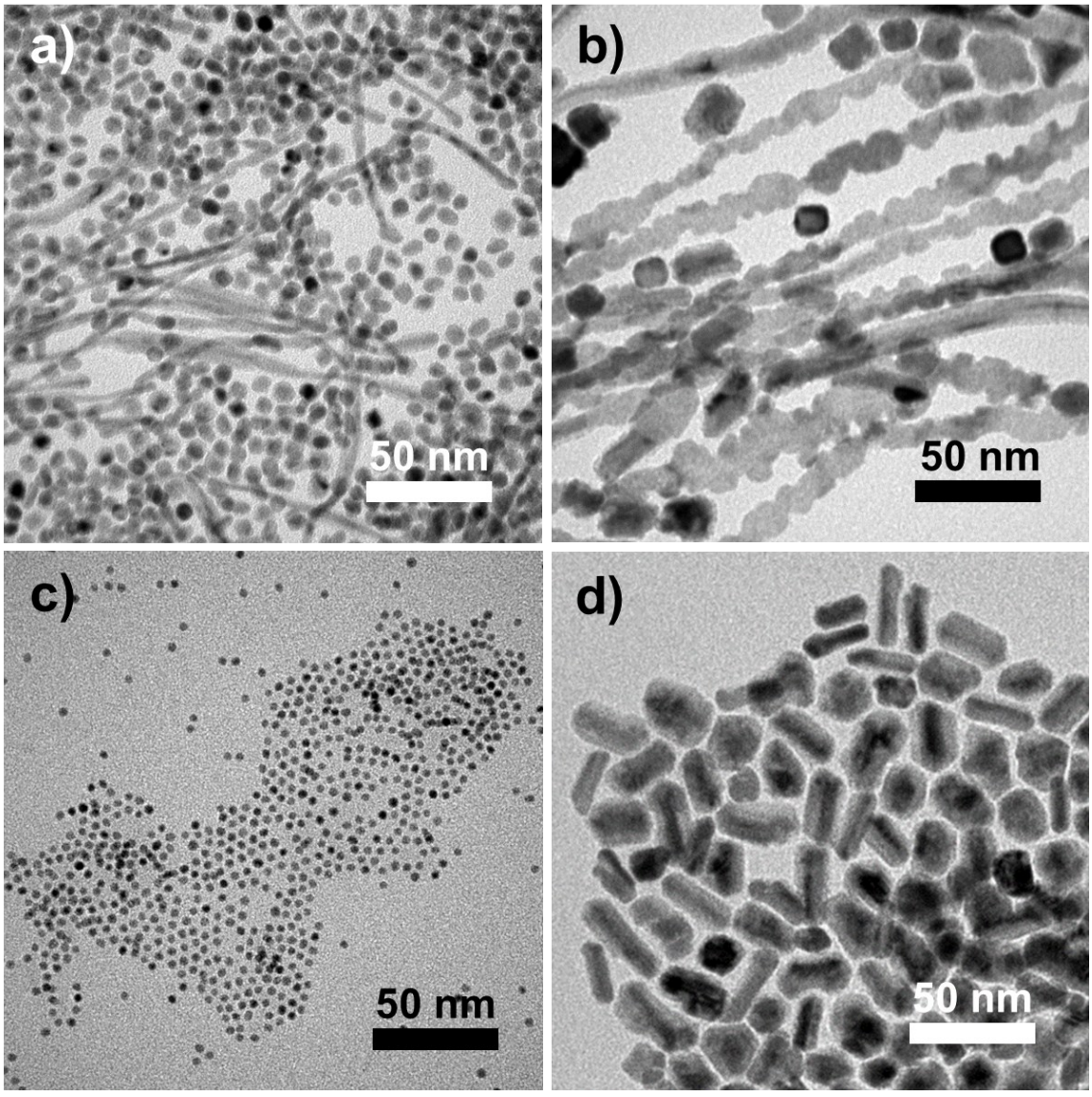

Fig. S6. Nanostructures obtained under various gas conditions. Atmospheric conditions in Schlenk tube are a) CO in aging step and Ar at 180 °C, b) Ar in aging step and CO at 180 °C, c) CO during the entire reaction, but without $Mo(CO)_6$, d) Ar in aging step and CO at 180 °C without $Mo(CO)_6$.

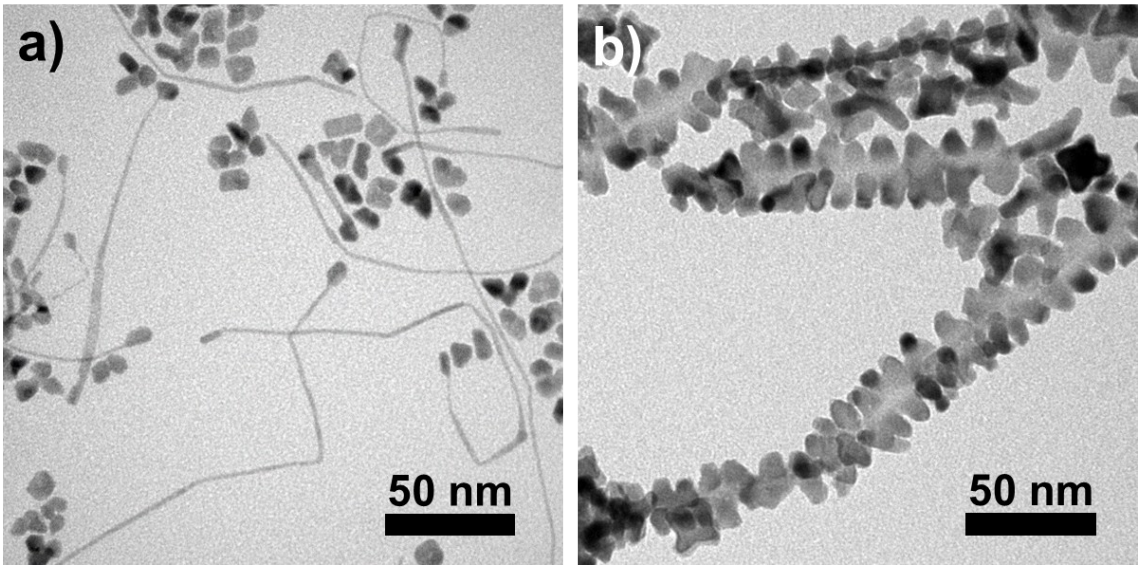

Fig. S7. TEM images of nanostructures synthesized without Ni precursor (Mo doped Pt dendritic nanowire; Mo-Pt DNW): a) intermediates after the aging step at 80 ^{o}C and b) Mo-Pt DNW.

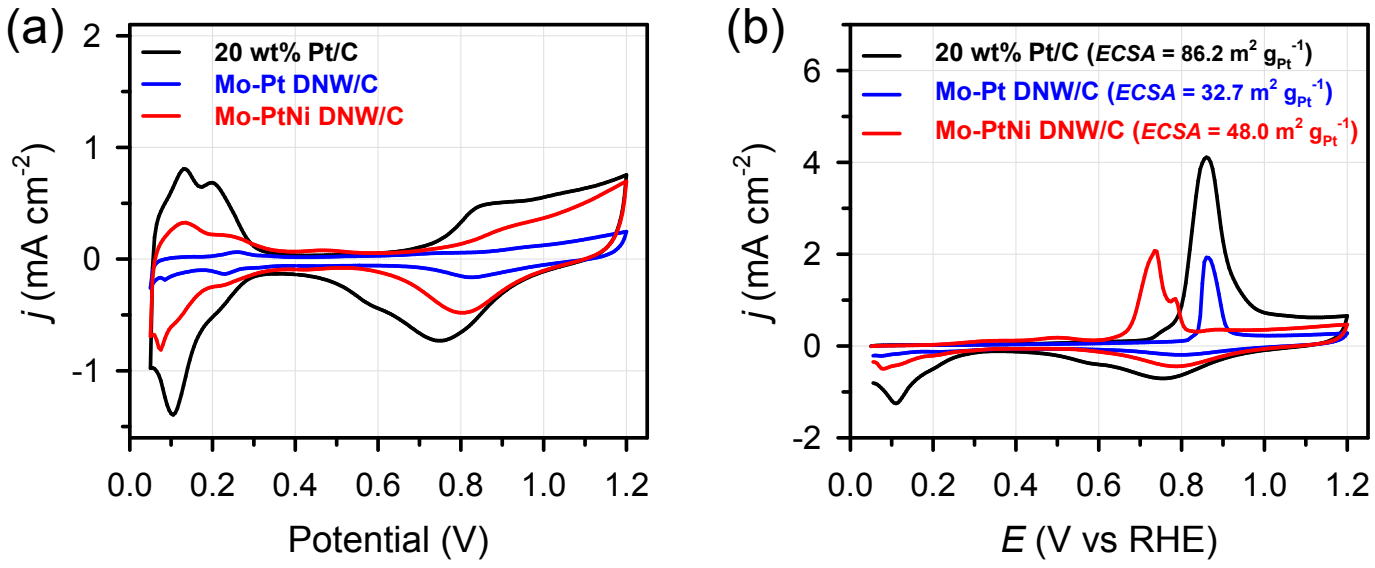

Fig. S8. a) Cyclic voltammograms of electrocatalysts. b) Electrochemically active surface area (ECSA) estimated by CO stripping method.

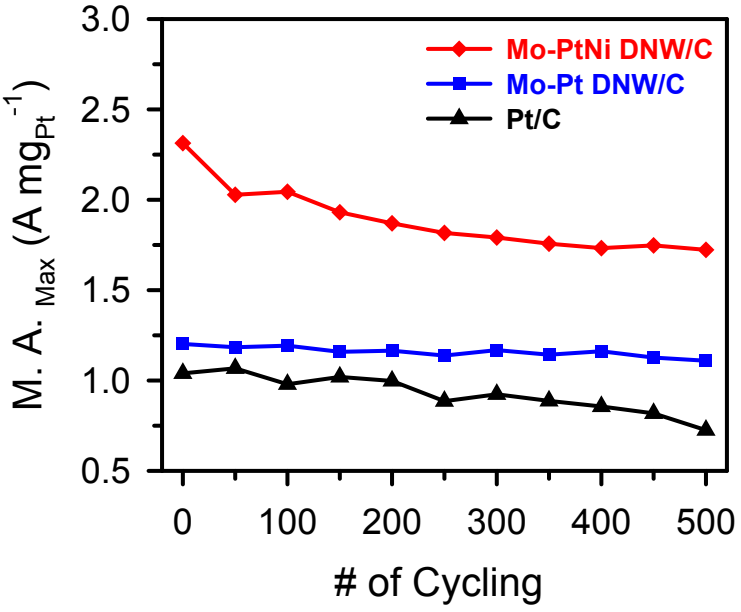

Fig. S9. MOR durability test with 500 potential cycling in the region of 0.05-1.20 V vs RHE.

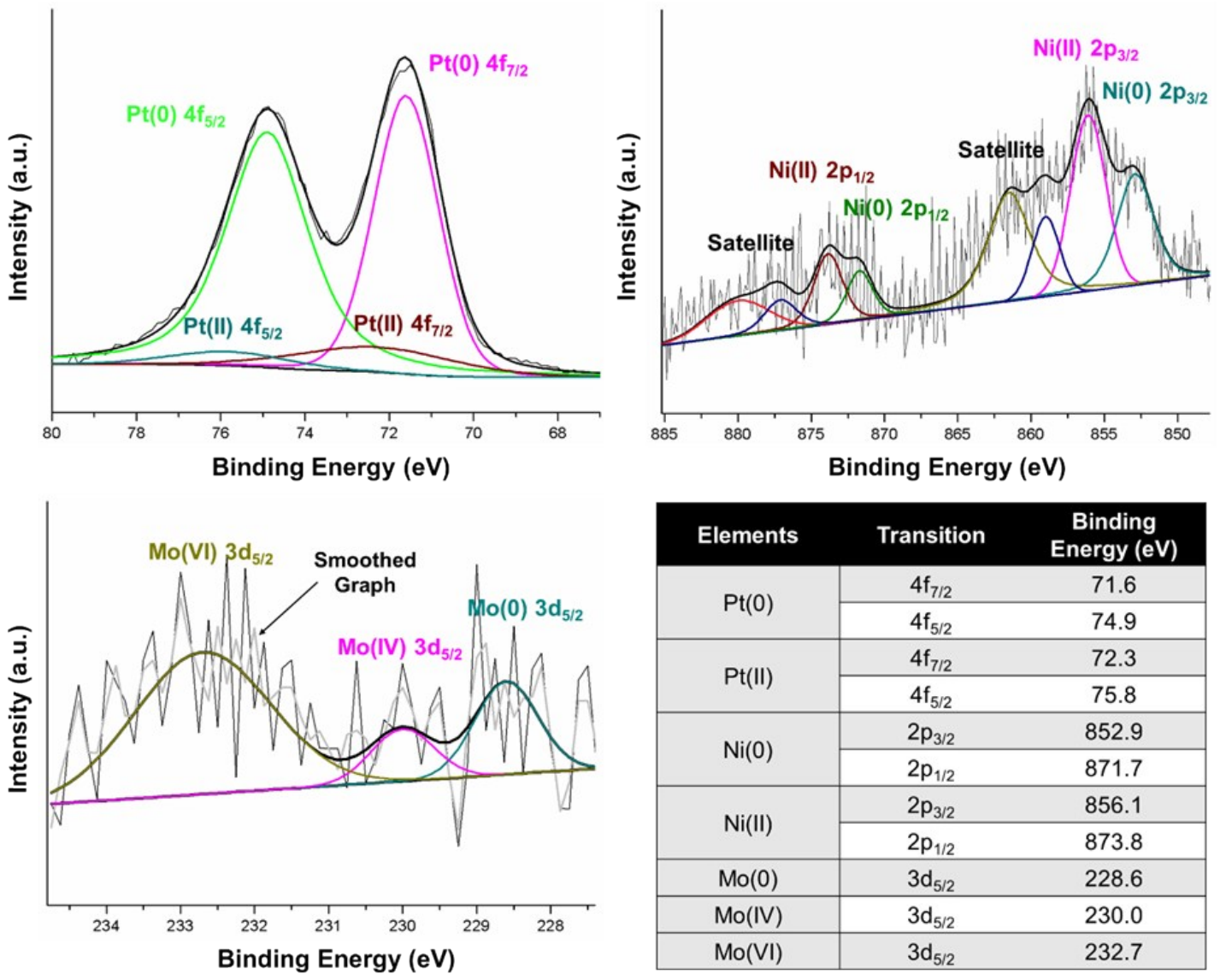

Elements	Transition	Binding Energy (eV)
Pt(0)	$4f_{7/2}$	71.6
	$4f_{5/2}$	74.9
Pt(II)	$4f_{7/2}$	72.3
	$4f_{5/2}$	75.8
Ni(0)	$2p_{3/2}$	852.9
	$2p_{1/2}$	871.7
Ni(II)	$2p_{3/2}$	856.1
	$2p_{1/2}$	873.8
Mo(0)	$3d_{5/2}$	228.6
Mo(IV)	$3d_{5/2}$	230.0
Mo(VI)	$3d_{5/2}$	232.7

Fig. S10. X-ray photoelectron spectroscopy (XPS) analysis of Mo-PtNi dendritic nanowire. Most of surface Pt in in metallic state and most of surface Ni and Mo species are in oxidized states. Notably, most of surface Mo species are Mo^{6+} and Mo^{4+} due to the formation of MoO_x.

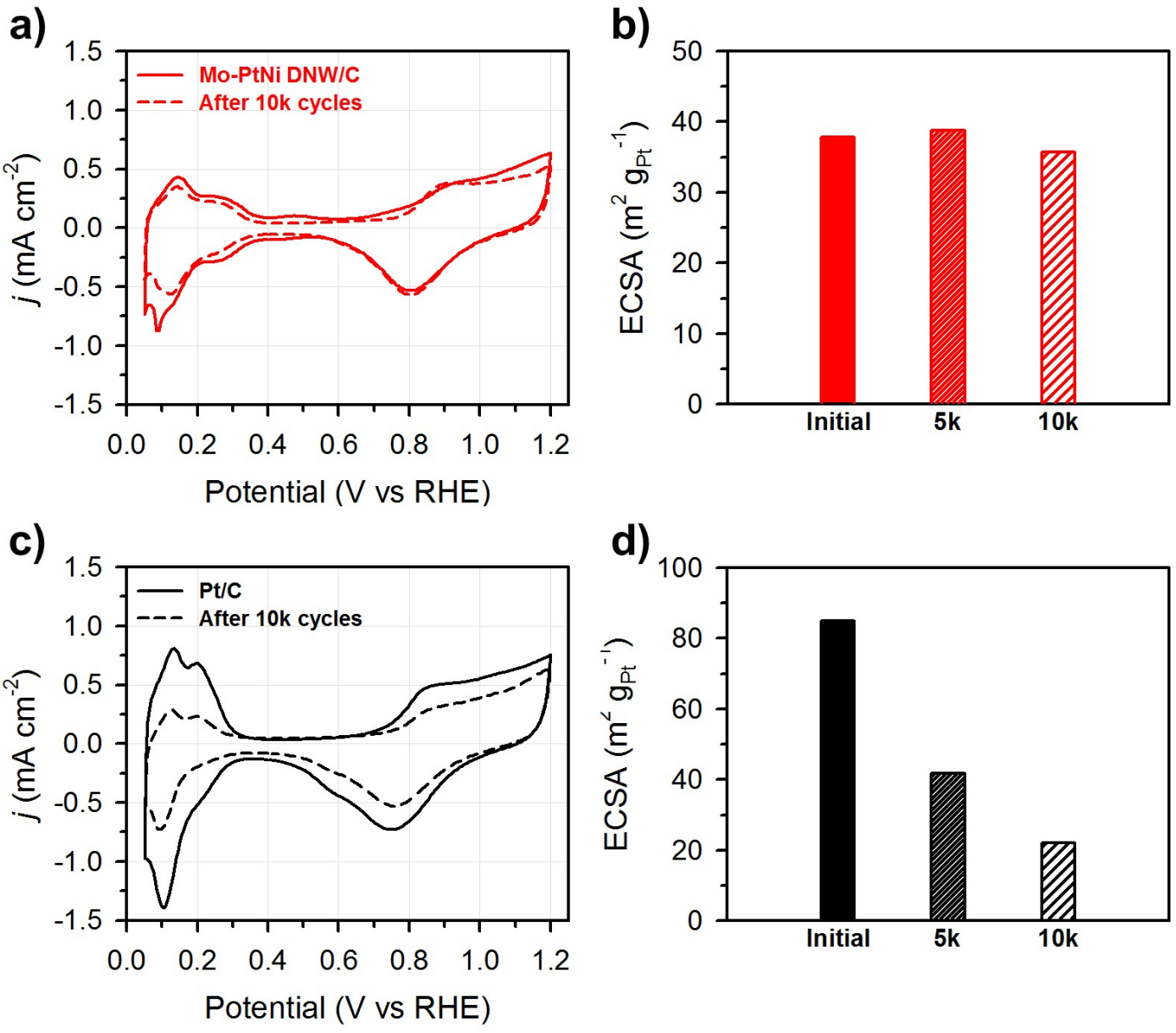

Fig. S11. (a) CV curves of Mo-PtNi DNW/C before and after an accelerated degradation test (ADT). (b) ECSAs of Mo-PtNi DNW/C for up to 10,000 ADT cycles. (c) CV curves of Pt/C before and after ADT. (d)) ECSAs of Pt/C for up to 10,000 ADT cycles.

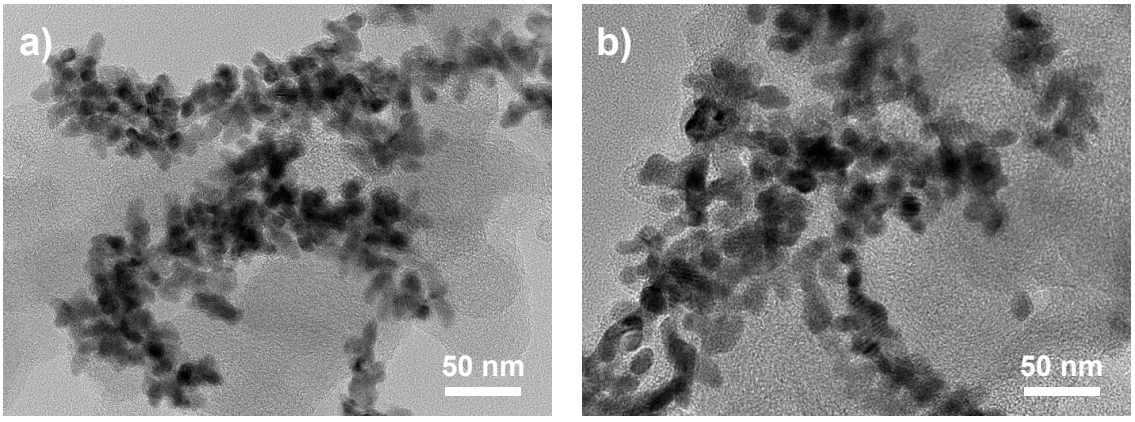

Fig. S12. (a) TEM image of Mo-PtNi DNW/C before the ADT. (b) TEM image of Mo-PtNi DNW/C after the ADT.

Table S1. Inductive coupled plasma-optical emission spectroscopy (ICP-OES) result of Mo-PtNi DNW/C. The quantitative analysis shows that nanostructure is composed of $Pt_{1.24}Ni$ with small amount of Mo-doping; 2.02 %.

	Pt	Ni	Mo
Weight %	25.61	6.28	0.48
Atomic %	54.82	43.16	2.02

Table S2. ICP-OES analysis data of Mo-Pt DNW. The nanostructure contains 2.04 % Mo, which is comparable to the doping level of Mo-PtNi DNW.

	Pt	Mo
Weight %	21.52	0.22
Atomic %	97.96	2.04

Table S3. ORR activity of Mo-PtNi DNW catalyst compared with those of previously reported Pt-based catalysts.

Catalyst	Loading	$E_{1/2}$	ECSA	Mass Activity	Specific Activity	Ref
	(μg_{Pt} cm^{-2})	(V)	(m^2 g_{Pt}^{-1})	(A mg_{Pt}^{-1})	(mA cm_{Pt}^{-2})	
Mo-PtNi DNW/C	**14.0**	**0.912**	**37.8 (H_{upd}) 48.0 (CO_{ad})**	**0.70**	**1.86 (H_{upd}) 1.46 (CO_{ad})**	**This work**
PtNi skeletal nanoframe/C	11.2	0.92	28	1.12	4.0	[1]
Mo-Pt_3Ni octahedra/C	4.08	0.95	67.7 (H_{upd}) 83.9 (CO_{ad})	6.98	10.3 (H_{upd}) 8.2 (CO_{ad})	[2]
Pt_3Ni nanoframe/C	-	0.94	66 (CO_{ad})	5.7	8.6 (CO_{ad})	[3]
Pt_5Gd	-	-	32	3.5	11	[4]
$Pt_{2.5}Ni$ octahedra/C	1.02	0.93	21 (H_{upd}) 31 (CO_{ad})	3.3	15.7 (H_{upd}) 10.6 (CO_{ad})	[5]
PtNi octahedra/C	8	0.92	43	1.65	3.8	[6]
PtNi octahedra/C	9.3	0.88	44	0.44	1.0	[7]
Pt_3Ni octahedra/C	3.0	0.85	-	0.11	2.8	[8]
Pt Octahedral nanocages/C	12.8	0.91	38.2	0.75	1.98	[9]
Pt_3Ni nanowire/C	2.5	0.96	43.4	4.15	9.56	[10]

[1] A. Oh, H. Baik, D. S. Choi, J. Y. Cheon, B. Kim, H. Kim, S. J. Kwon, S. H. Joo, Y. Jung and K. Lee, *ACS Nano*, 2015, **9**, 2856–2867.

[2] X. Huang, Z. Zhao, L. Cao, Y. Chen, E. Zhu, Z. Lin, M. Li, A. Yan, A. Zettl, Y. M. Wang, X. Duan, T. Mueller and Y. Huang, *Science*, 2015, **348**, 1230–1234.

[3] C. Chen, Y. Kang, Z. Huo, Z. Zhu, W. Huang, H. L. Xin, J. D. Snyder, D. Li, J. A. Herron, M. Mavrikakis, M. Chi, K. L. More, Y. Li, N. M. Markovic, G. A. Somorjai, P. Yang and V. R. Stamenkovic, *Science*, 2014, **343**, 1439–1443.

[4] M. Escudero-Escribano, P. Malacrida, M. H. Hansen, U. G. Vej-Hansen, A. Velázquez-Palenzuela, V. Tripkovic, J. Schiøtz, J. Rossmeisl, I. E. L. Stephens, and I. Chorkendorff, *Science*, 2016, **352**, 73–76.

[5] S.-I. Choi, S. Xie, M. Shao, J. H. Odell, N. Lu, H.-C. Peng, L. Protsailo, S. Guerreor, J. Park, X. Xia, J. Wang, M. J. Kim and Y. Xia, *Nano Lett.*, 2013, **13**, 3420–3425.

[6] C. Cui, L. Gan, M. Heggen, S. Rudi and P. Strasser, *Nat. Mater.*, 2013, **12**, 765–771.

[7] J. Wu, A. Gross and H. Yang, *Nano Lett.*, 2011, **11**, 798–802.

[8] J. Zhang, H. Yang, J. Fang and S. Zou, *Nano Lett.*, 2010, **10**, 638–644.

[9] L. Zhang, L. T. Roling, X. Wang, M. Vara, M. Chi, J. Liu, S. -I. Choi, J. Park, J. A. Herron, Z. Xie, M. Mavrikakis and Younan Xia, *Science*, 2015, **349**, 412–416.

[10] L. Bu, J. Ding, S. Guo, X. Zhang, D. Su, X. Zhu, J. Yao, J. Guo, G. Lu and X. Huang, *Adv. Mater.*, 2015, **27**, 7204–7212.